ELSEVIER

Temperature dependence of strain hardening and plastic instability behaviors in austenitic stainless steels

T.S. Byun *, N. Hashimoto, K. Farrell

Metals and Ceramics Division, Oak Ridge National Laboratory, P.O. Box 2008, MS-6151, 1 Bethel Valley Road, Ms-6151 Oak Ridge, TN 37831, USA

Abstract

The temperature dependencies of true strain-hardening and plastic-instability properties are investigated for austenitic stainless steels; including annealed 304, 316, 316LN, and 20% cold-worked 316LN, at test temperatures from −150 to 450 °C. In both annealed and cold-worked conditions, strength decreases with increasing temperature, while ductility peaks below room temperature and is least at about 400 °C. At room temperature or below, the strain-hardening behavior exhibits two stages consisting of a rapid decrease for small strains and an increase-decrease cycle before plastic instability occurs. At higher temperatures the strain-hardening rate decreases monotonically with strain. The characteristics of these strain-hardening behaviors are explained by changes in deformation microstructure. Transmission electron microscopy (TEM) of the deformed 316LN steel shows that twins, stacking faults, and/or martensite laths, along with dislocations, are formed at subzero temperatures, and dislocation-dominant microstructures at elevated temperatures. It is also shown that the average strain-hardening rate during necking to failure is almost equal to the true stress at the onset of necking. This stress is called the plastic instability stress (PIS). Cold-worked specimens fail by prompt necking at yield when the yield stress exceeds the PIS of annealed material, indicating that the PIS is independent of prior cold work.

1. Introduction

The 300 series austenitic stainless steels provide high resistance to corrosion and oxidation and retain high strength and excellent ductility over a temperature range from cryogenic to elevated temperatures [1,2]. Such favorable properties enable those steels to meet requirements for application in nuclear facilities such as fission and fusion reactors [3–12] and accelerator-based systems [13–19], as well as for a wide variety of non-nuclear applications [1]. Their high resistance to degradation by irradiation is particularly important for nuclear applications. Therefore, the austenitic stainless steels, which show extraordinary high ductility before irradiation, have been candidates for many in-reactor structures

[3–6]. As an example for recent nuclear application, the 316LN stainless steel was selected as the primary candidate material for the mercury container vessel of the spallation neutron source (SNS) facility [13–15,18,19]. The selection was based on R&D from the fusion materials program [7,8,20]. In the present study three 300 series stainless steels, annealed 316, annealed and 20% cold-worked 316LN, and annealed 304 stainless steels have been tested over the temperature range −150 to 450 °C to supply baseline data for design activity for the SNS target vessel and to use the data for further analysis on plastic instability behavior.

Since the austenite phase in the 300 series stainless steels is thermodynamically stable over a wide range of temperature, it can be hardened only by cold working if the alloy composition is not modified to introduce precipitates [1,2]. It has been shown that the effects of plastic deformation, by either cold working before tensile testing or the tensile testing itself, resembled those of

---
* Corresponding author. Tel.: +1-865-576-7738; fax: +1-865-574-0641.

E-mail address: byunts@ornl.gov (T.S. Byun).

irradiation [21,22]. Further, since the degradation of mechanical properties by irradiation in those steels rely on the excellent initial ductility, the loss of ductility and embrittlement by irradiation are known to be relatively small when compared to other metallic materials [13,15,18]. These facts indicate that their response to plastic deformation prior to irradiation might supply much of the information needed to predict the material performance after irradiation. Therefore, discussions in the present paper are focused on the temperature dependence of stress–strain behavior before irradiation and on the elucidation of the differences and similarities between irradiated and deformed conditions.

2. Experimental

The test materials consisted of four austenitic stainless steels: annealed 304, 316, and 316LN stainless steels, and a 20% cold-worked 316LN stainless steel. The chemical compositions and thermo-mechanical histories of the materials are listed in Table 1. A flat, sub-sized tensile specimen design, so-called SS-3 type [19], was used for the present experiments. Its gage section dimensions are 7.62 mm long, 1.5 mm wide and 0.75 mm thick.

Tensile tests were performed using a screw-driven Tinius–Olsen machine at a nominal strain rate of 10^{-3} s^{-1}. Test temperature ranged from −150 to 450 °C, and it was controlled by an automatic heating/cooling chamber system using electrical heating and liquid nitrogen injection. Engineering stress–strain and true stress–true strain data were calculated from the load–displacement measurements.

After tensile failure, the dimensions of the neck, width and thickness at the point of the smallest cross-sectional area, were measured using a high-precision micrometer to obtain the final cross-sectional area A_F. True fracture strain ε_F and true fracture stress σ_F were calculated from the initial and final cross-sectional areas, A_0 and A_F, respectively, and fracture load P_F by the following relationships [23]:

$$\varepsilon_F = \ln(A_0/A_F), \tag{1}$$

$$\sigma_F = P_F/A_F. \tag{2}$$

Then, the average strain-hardening rate during necking, HRN, was calculated by

$$HRN = \frac{(\sigma_F - PIS)}{(\varepsilon_F - \varepsilon_U)}, \tag{3}$$

where ε_U is the true uniform strain.

For microstructural observations, 1.5 mm long pieces (roughly squares) were cut from the uniform deformation sections of annealed 316LN tensile samples and were ground to a thickness of about 0.2 mm or less. The thin square plates were then thinned to perforation by a twin-jet electrochemical polisher and deformation microstructures were observed in a JEOL-2000FX transmission electron microscope operating at 200 kV.

3. Results and discussion

3.1. Temperature dependence of engineering tensile properties

Figs. 1–4 present selected engineering stress–strain curves for the four austenitic stainless steels. These steels showed strong temperature dependencies of strength and ductility; the strength increased as test temperature decreased. Contrary to most other metals, the ductility did not decline systematically with decreasing temperature rather it peaked between −100 °C and room temperature (20 °C). Except for the 20% cold-worked specimens tested at room temperature or higher, tensile specimens showed high uniform elongations of 40–100% and relatively small necking elongations. (Hereafter the engineering strain is expressed in percent (%) to distinguish it from the true strain in fraction.) At about 100 °C or higher, the 20% cold-worked 316LN stainless steel showed prompt necking at yield, resulting in zero uniform ductility.

The other remarkable feature of the temperature dependence is the change in curve shape with test temperature. Above room temperature, except for some of the 20% cold-worked 316LN specimens showing prompt necking at yield, the engineering stress increased

Table 1
Compositions and thermo-mechanical treatments for austenitic stainless steels

Material[*]	Composition (wt. %)									
	Fe	Ni	Cr	Mo	Mn	Si	P	C	N	Others
316LN-annealed and -cold worked	Bal.	16.3	10.2	2.01	1.75	0.39	0.029	0.009	0.11	
316-annealed	Bal.	17.15	13.45	2.34	1.86	0.57	0.024	0.059	0.031	0.018 S, 0.1Cu, 0.02 Co
304-annealed	Bal.	18.37	8.04	0.04	1.73	0.44	0.022	0.036	0.058	0.03Co, 0.1Cu, 0.12V
316LN–20% CW	Bal.	16.3	10.2	2.01	1.75	0.39	0.029	0.009	0.11	

[*] Samples annealed at 1050 °C for 30 min after machining; cold-worked samples were machined from a sheet that was 20% cold-rolled from a 1-mm thick sheet. Tensile specimens were made in the rolling (longitudinal) direction.
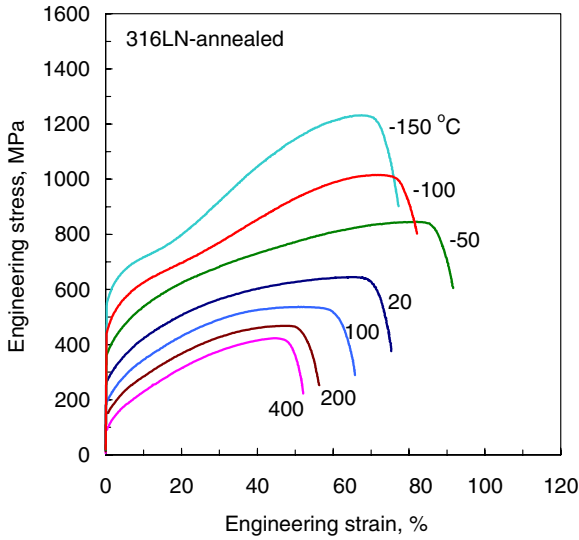
Fig. 1. Temperature dependence of the engineering stress–strain curves for annealed 316LN stainless steel.
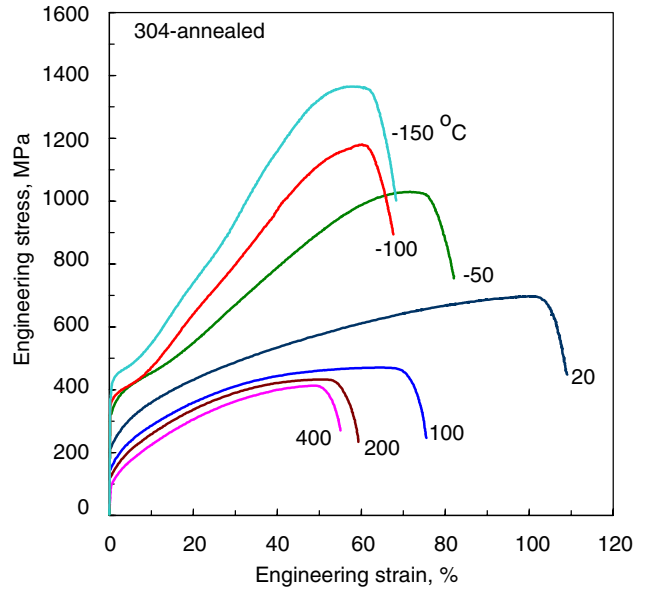

Fig. 3. Temperature dependence of the engineering stress–strain curves for annealed 304 stainless steel.
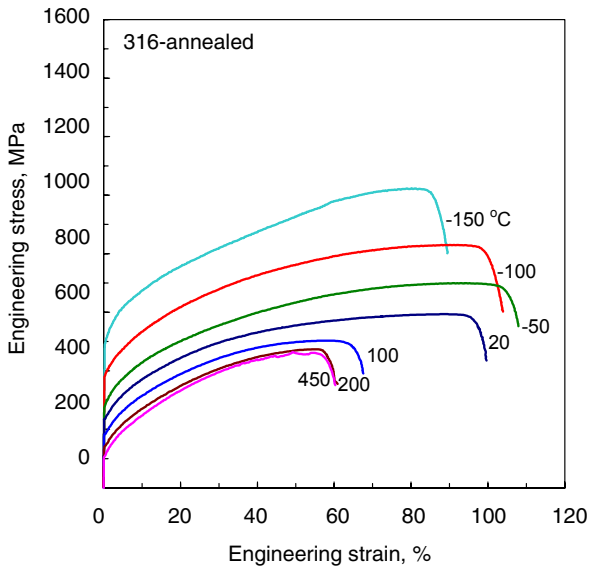

Fig. 2. Temperature dependence of the engineering stress–strain curves for annealed 316 stainless steel.
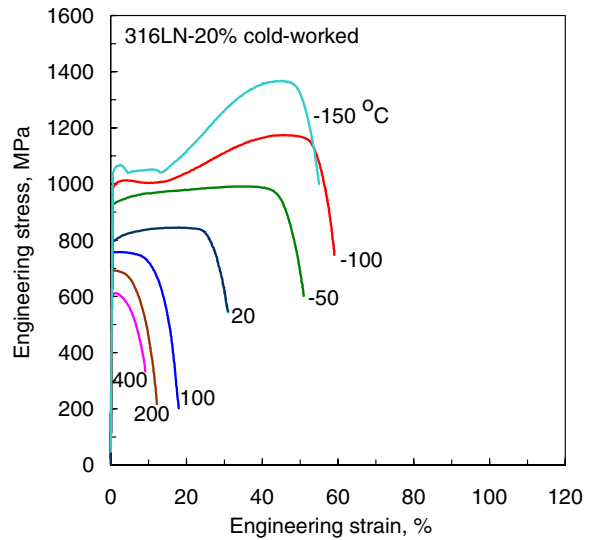

Fig. 4. Temperature dependence of the engineering stress–strain curves for 20% cold-worked 316LN stainless steel.

monotonically with engineering strain until necking intervened. At −50 °C or below, however, the austenitic steels showed two-stage hardening behavior; the initial parabolic hardening stage, where strain-hardening rate decreased with strain, ending at an engineering strain between 3% and 20%, and an increase-decrease cycle of strain-hardening rate in a second hardening stage. For the 20% cold-worked 316LN steel at −100 and −150 °C, the strain hardening in the initial hardening stage was so low that it looked like Lüders region. Due to the acceleration of strain hardening in the second stage, the necking occurred at fairly high stress and strain levels. Also, the average strain-hardening rate seemed to be

higher at lower temperatures, where strength was higher. In general, the average strain-hardening rate decreased with strength [18,19]. This characteristic strain-hardening behavior, in relation to microstructural change, will be explored again in later sections. Among the test materials, the annealed 316 steel displayed the weakest temperature dependence in the curve shape.

Engineering strength data are presented in Fig. 5. Both yield strength (YS) and ultimate tensile strength (UTS) increased with decreasing temperature. In the annealed steels, the yield strengths at −150 °C were in the range 430–570 MPa, or 4.3–5.6 times those at 400 °C
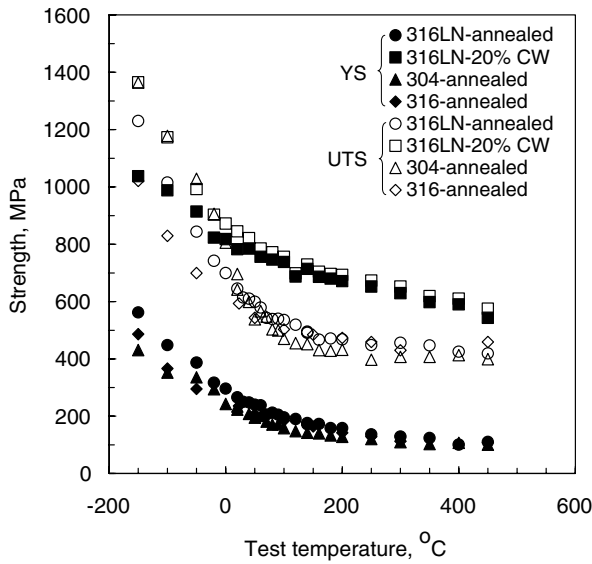
Fig. 5. Temperature dependence of the strength of stainless steels.

(100–110 MPa). In the cold-worked stainless steel, however, the temperature dependence of YS was much smaller; the yield strength at −150 °C is 1040 MPa, less than 2 times that at 400 °C (590 MPa). The UTS displayed less significant temperature dependence than YS; for all tested materials, the ultimate tensile strengths at −150 °C were in the range 1000–1400 MPa, whereas those at 400 °C were 400–610 MPa. Excluding the cold-worked material, the difference in the strength between the test materials was reduced a little at elevated temperatures.

Fig. 6 displays the temperature dependence of elongations. This figure shows that the uniform and total elongations (UE a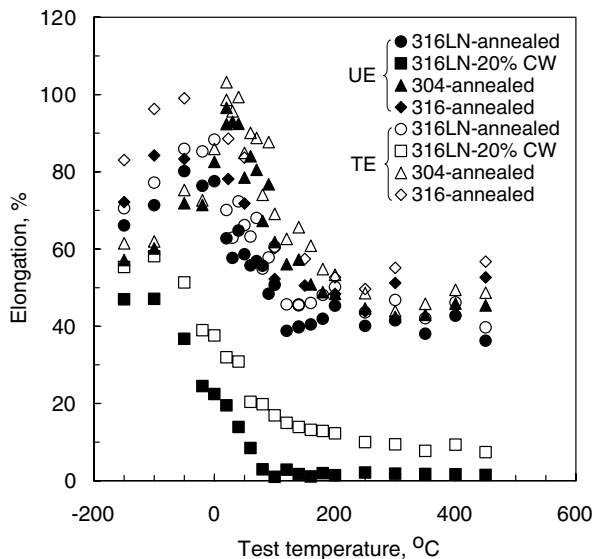nd TE, respectively) of anneal steels have maxima of over 80% below room temperature. A rapid decrease of ductility occurred as the test temperature was increased from the maximum ductility temperature to about 200 °C. All annealed steels retained more than 40% elongations at 400 °C. As shown in the engineering stress–strain curves in Figs. 1–4, the strength fell rapidly once the deformation reached plastic instability. Consequently, the necking strain, which is the difference between UE and TE, was only 5–10% in the annealed steels. In the 20% cold-worked 316LN steel, on the other hand, the UE and TE values were much lower than those of the annealed steels but the necking strains were the same or slightly larger than those for the annealed steels. For the 20% cold-worked 316LN at −100 °C, UE and TE had maxima of 52 and 62%, respectively. UE decreased with temperature and became nearly zero at 100 °C or higher.

3.2. Temperature dependence of strain-hardening behavior

Figs. 7–10 present the true stress (σ) vs. true strain (ε) curves and the strain-hardening rates ($d\sigma/d\varepsilon$) vs. true strain curves at selected temperatures. In annealed 316LN stainless steel, Fig. 7, the true stress–true strain curves at 20 and 400 °C decreased monotonically with strain in the uniform deformation region. Very high strain-hardening rates were found at the onset of deformation, and the strain-hardening rate immediately decreased rapidly with strain in the true strain range 0–0.1. However, despite this decrease, the strain the strain-hardening rate remained above the true stress value until plastic instability occurred. It is also notable that the strain-hardening rate again drops rapidly as the deformation approaches the plastic instability point
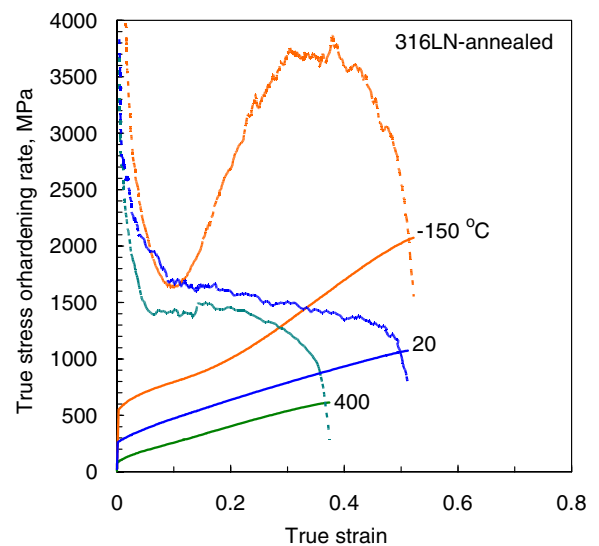

Fig. 6. Temperature dependence of the ductility of stainless steels.

Fig. 7. Temperature dependence of the true stress–true strain curve (continuous line) and strain-hardening rate (dotted line) in annealed 316LN stainless steel.

Fig. 8. Temperature dependence of the true stress–true strain curve (continuous line) and strain-hardening rate (dotted line) in annealed 316 stainless steel.

Fig. 10. Temperature dependence of the true stress–true strain curve (continuous line) and strain-hardening rate (dotted line) in 20% cold-worked 316LN stainless steel.
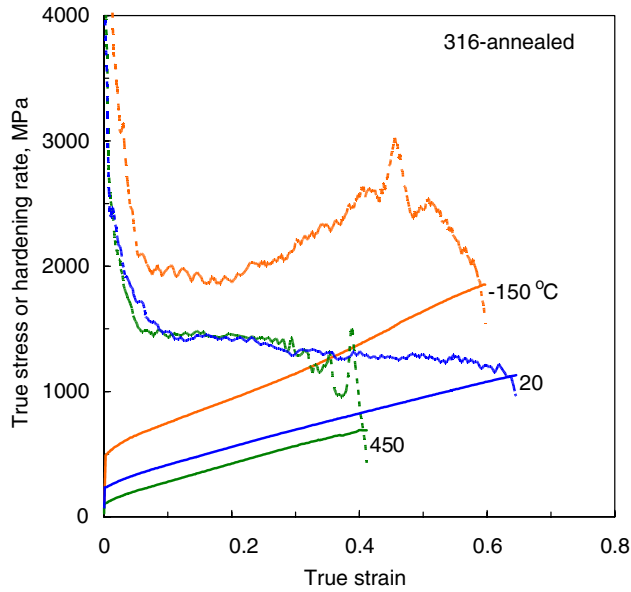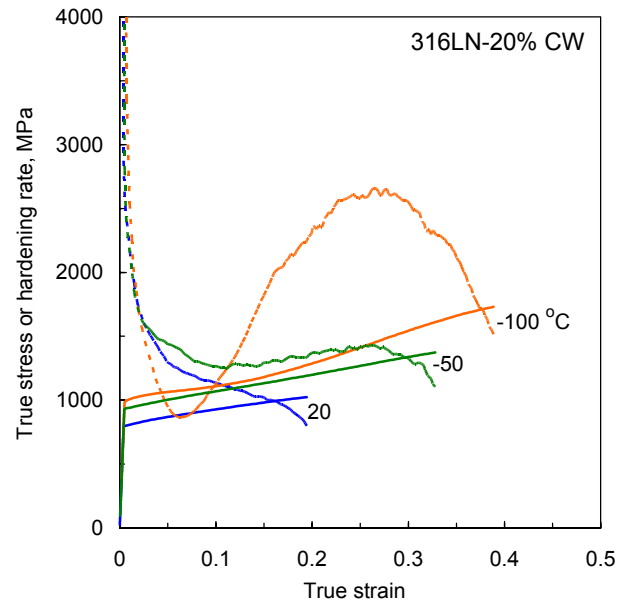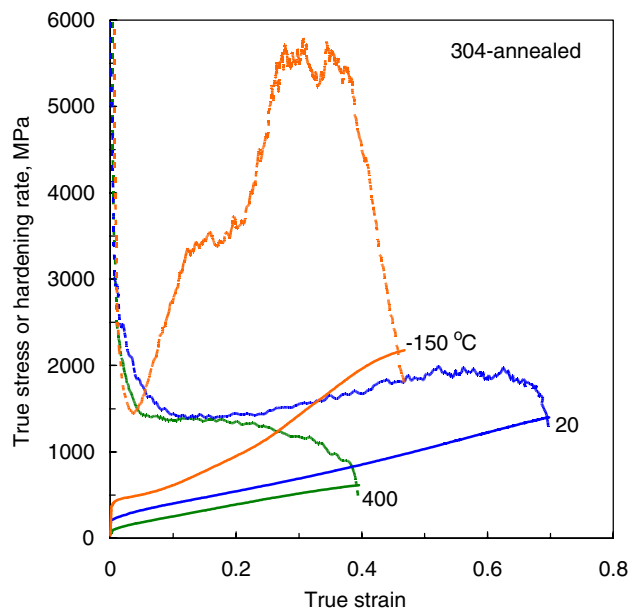

Fig. 9. Temperature dependence of the true stress–true strain curve (continuous line) and strain-hardening rate (dotted line) in annealed 304 stainless steel.

where necking is initiated at the intersection of the curves of σ vs. ε and dσ/dε vs. ε, which corresponds to the engineering UTS [23,24]. The instability strain, or uniform strain, was higher when the overall strain-hardening rate was higher. At −150 °C the strain-hardening curve displayed a two-stage hardening behavior. The first parabolic hardening trend ended at a strain of about 0.1, where the strain-hardening rate curve had a

minimum of about 1700 MPa. From this point, the strain-hardening rate increased with strain and reached 3800 MPa level at a strain of about 0.3. A plateau at a high strain-hardening rate of about 3800 MPa was formed in a strain range of 0.3–0.45, and then the strain-hardening rate decreased rapidly to the intersection with the true stress–true stain curve. In the first parabolic-hardening region the rapidly decreasing strain-hardening rates were similar for the three temperatures. In the higher strain range (>0.1), however, the strain-hardening rate at −150 °C was very much higher than those at 20 and 400 °C. This higher strain-hardening rate at −150 °C resulted in plastic instability occurring at a higher strain, as indicated in the UE data in Fig. 6. In the annealed 316LN stainless steel the two-stage hardening behavior is present at −50 °C or below.

For the other two annealed stainless steels, type 316 and 304 stainless steels, Figs. 8 and 9, the overall temperature dependencies of σ vs. ε and dσ/dε vs. ε curves were similar to those of the annealed 316LN stainless steel. In detail, however, the temperature dependence of dσ/dε vs. ε curve was stronger in the annealed 304 stainless steel than in the annealed 316LN stainless steel. In the second hardening stage of the 304 steel at −150 °C, the maximum value of dσ/dε was at 5700 MPa level, which was considerably higher than those of 316LN and 316 steels. Despite this clear two-stage hardening at low temperatures, a relatively weak two-stage hardening behavior was observed at room temperature. The maximum value of dσ/dε for the annealed 316 steel at −150 °C was only about 3000 MPa, the lowest among the annealed materials.

The temperature dependencies of the vs. ε curve and dσ/dε vs. ε curve in the 20% cold-worked 316LN steel, Fig. 10, appeared to be less significant when compared to the annealed 316LN stainless steel. Although the overall strain-hardening rate was lower than those of the annealed steels, the second stage hardening was still high at −100 °C or below. An interesting point is that at −100 °C the dσ/dε vs. ε curve intercepts the σ vs. ε curve at a strain of 0.04 without causing gross plastic instability. Further, the strain-hardening rate increased again after it reached a minimum at a strain of 0.07. A feature of this behavior is that the declining strain-hardening rate was already beginning before the interception occurred, and it accelerated soon after the interception. The incipient neck was thus stopped and erased before it affected the stress–strain behavior significantly. At this temperature, the maximum value for dσ/dε in the second stage was about 2600 MPa, and finally plastic instability or necking occurred at a large true strain of 0.38.

3.3. Deformation microstructures

Significant variations in the strain-hardening behavior shown in Figs. 7–10 must result from changes in the deformation mechanisms. Fig. 11 displays significant differences in TEM microstructures after deformation to 5%, 20%, and 50% engineering strain at −150 and 200 °C. At −150 °C many thin twins or stacking faults along with perfect dislocations were formed during early deformation up to 5% strain, Fig. 11(a). Formation of those microstructures corresponds to the parabolic stress–strain response in Fig. 7. Fig. 11(b) shows many twins have formed during deformation to 20%; additionally, dense tangled dislocations, seen as dark patches (some of these may be martensite particles), became
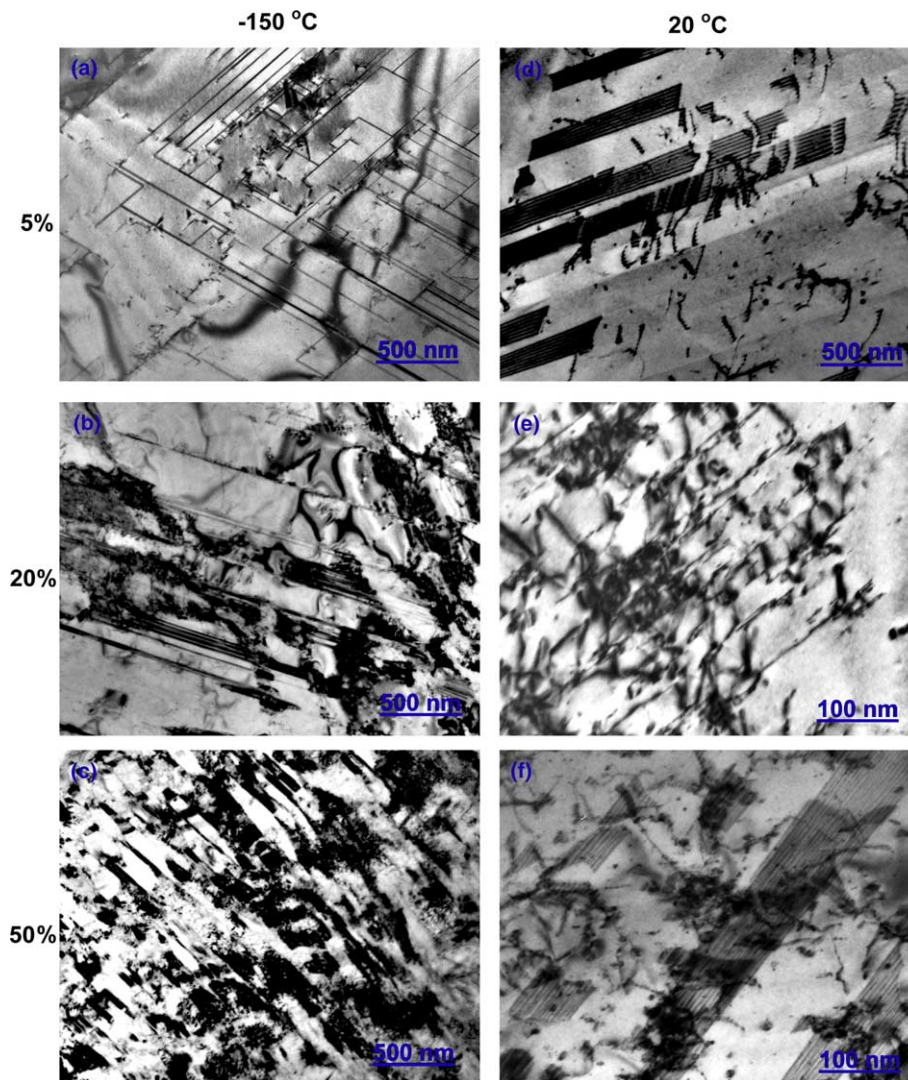

Fig. 11. Temperature and strain dependence of deformation microstructure in annealed 316LN stainless steel after deformation to (a) 5%, (b) 20%, and (c) 50% at −150 °C, and to (d) 5%, (e) 20%, and (f) 50% at 200 °C (zone axis = [0 1 1]).

abundant. Dense tangled dislocations are needed to accommodate a large bulk strain of 20% (about 0.182 true strain) because the thin twins can account for only part of the bulk strain. The volume fraction of the twin layers in Fig. 11(b) was measured at about 0.09. It is known that the theoretical shear strain within a twin layer formed on a {1 1 1} plane is 0.707 [25,26], which equals 0.354 in the equivalent strain unit. Therefore, the twins in Fig. 11(b) account for only a small amount of strain, 0.032 ($=0.09 \times 0.354$), at a bulk strain of 0.182.

Fig. 11(c) shows a microstructure after heavy deformation to 50%. Deformation to this strain level produced complicated microstructures; which included heavily tangled dislocations, twins, stacking faults, and martensite. Lath structure in the martensite region with a width of order 100 nm is evident. The temperature for the start of the strain-induced austenitic to martensite transformation is unknown for the 316LN alloy; however, the austenite phase is believed to be thermodynamically stable at −150 °C because no martensite was found in Fig. 11(a). An effect of stress on the martensitic transformation in the austenitic stainless steels is normally to raise the martensite start temperature, which means that deformation can stimulate martensite formation at a given temperature [27]. It is reported [28,29] that martensite is frequently observed after deformation at room temperature or below; ε-martensite was formed along with stacking faults, while α-martensite nucleation seemed to be associated with dislocation pileups where the stress level was very high. The true stresses corresponding to the microstructures in Fig. 11(a)–(c) were 700, 1000, and 2100 MPa, respectively. The martensite in Fig. 11(c), which has been formed with the aid of high stresses up to 2100 MPa, is believed to be mostly α-martensite.

At an elevated temperature of 200 °C the deformation microstructures consisted of tangled dislocations along with a single-layer or overlapped stacking faults, Figs. 11(d)–(f). No martensite was found in these microstructures, which were formed in the stress range 400–1100 MPa. Both individual and pile-up dislocations dissociated into partials to form stacking fault segments. The dominant microstructure seems to be tangled dislocations.

Uniform ductility can be a measure of a material's ability to avoid a strain localization that will eventually lead to a shear failure. Austenitic stainless steels usually show excellent uniform ductility, especially at cryogenic temperatures, and it comprises the major part of the total ductility. This excellent uniform ductility of the face-centered cubic steels has been explained by various deformation mechanisms originating from low stacking fault energy (SFE < 20 mJ/m^2) [24–26,30–35]. With such a low SFE a gliding ordinary (perfect) dislocation actually consists of two dissociated partial dislocations with an equivalent separation on the order of 10 nm

[25–35]. This separation increases as the applied stress increases by strain hardening [31,34–37]. A stacking fault exists formed between the partials, which makes cross-slip difficult because the stacking fault must be eliminated for the dislocation to cross slip. Therefore, the gliding dislocations are confined to a thin slip band forming a large pile-up against an obstacle, most likely a grain boundary. Large pile-ups can build a large long-range back stress and result in high strain-hardening rate [23–26]. Also, the formation of large stacking faults and mechanical twins is easier in the low SFE metals such as stainless steels. Progressive formation of stacking faults and twins on intersecting planes during deformation means that obstacles to later glides also increase progressively during deformation. This should produce a high strain-hardening rate [18]. During deformation at a high strain-hardening rate, the plastic deformation can spread into a larger volume of material, and thus the strain localization or necking is delayed. In high stacking fault energy materials, cross-slip can occur easily, and therefore tangled dislocation structures are developed in relatively early stage, which results in early saturation at relatively low uniform ductility [24]. Cross-slipping and tangled dislocations may also encourage annihilation of dislocations by increasing the possibility for dislocation–dislocation interactions [38].

The above explanation associated with dislocation separation of partial dislocations may account for the high uniform ductility of the austenitic stainless steels. However, it can not explain the re-acceleration of strain-hardening rate from 5–20% strain and even higher strain-hardening rate in the second hardening stage at −50 °C or below. It is believed that the martensite transformation is responsible for the re-acceleration of strain-hardening and resultant high uniform ductility at low temperatures. As seen in Fig. 11(c), fine martensite laths of ∼10 nm were formed during deformation and those should reduce effective grain size to a large degree from the original grain size of about 30 μm. Further, since the martensite transformation is a stress (or strain)-assisted transformation in the 316LN steel, the volume fraction of martensite might increase with strain and stress. Therefore, as a similar role of twinning in deformation [24–26,28–37], a progressive formation of obstacles, martensite laths and their boundaries, might supply a less exhaustible hardening mechanism. Also, similar mechanical and microstructural behaviors are found in the Fe–Mn–Si–Al steels or so-called the TRIP/TWIP steels (transformation/twinning induced plasticity steels) [39–41]. Overall, the uniform ductility should increase when more stress-induced obstacles such as large stacking faults, twins, and martensite laths are formed during deformation, while less uniform ductility will be measured when a tangled dislocation network is dominant [18,21,22].

3.4. Strain-hardening behavior during plastic instability

Considere's criterion for plastic instability [18,23,24], $\sigma = d\sigma/d\varepsilon$, was used to determine the true stress at the onset of necking, i.e., the plastic instability stress (PIS) [21,22]. When the Considere's criterion is satisfied, the two curves, σ vs. ε curve and $d\sigma/d\varepsilon$ vs. ε curve, intersect each other at the uniform true strain, ε_U. In case that the two curves meet more than once (e.g., the −100 °C case in Fig. 10), the highest strain interception is regarded as the onset of necking. The temperature dependence of PIS is presented in Fig. 12, along with that of average strain-hardening rate during necking (HRN).

The PIS decreased rapidly with temperature in the temperature range −150 to 100 °C and was almost flat over a temperature range 100–450 °C. This response is similar to the temperature dependencies of YS and UTS. It is worth noting that the four different stainless steels show similar PIS values, in spite of the differences in the other tensile properties. In particular, similar PIS values were obtained for both annealed and 20% cold-worked 316LN steels, which indicated that PIS was not affected by the pre-strain applied at lower temperature. Similar behavior has been observed in irradiated materials; PIS had little dependence on irradiation dose [21,22], i.e., on degree of radiation hardening. These observations indicate that similar PIS values will be obtained in different material conditions: annealed, irradiated, and pre-strained conditions. This leads to the conclusion that irradiation and pre-strain produce similar effects on plastic deformation. Temperature change, on the other hand, can have significant influence on PIS as well as on the strength of the material, as seen in Fig. 12.
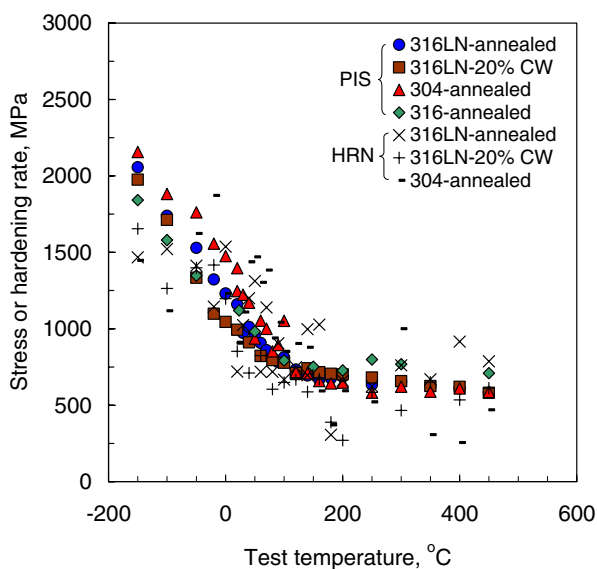
To compare the strain-hardening behaviors before and after the onset of necking, the values for average HRN were evaluated by Eq. (3) for the annealed 316LN, 20% cold-worked 316LN, and annealed 304 steels. The HRN data are overlaid on the PIS data in Fig. 12. This comparison reveals that the magnitude and temperature dependence of HRN are approximately the same as those of PIS over the test temperature range. It has been confirmed that the strain-hardening rate is positive during necking in both irradiated and unirradiated materials although the engineering stress decreases with elongation [19,21,22,42–44]. This is believed to be valid as long as there is a diffused neck, which occurs usually in ductile metals before a final failure by localized shear (banding) or cleavage initiation. The present result indicates an additional aspect of necking deformation that is not generally appreciated, namely that, although the strain-hardening rate is low, it remains nearly unchanged during necking process. This conclusion assumes that during necking deformation the true stress–true strain curve will be a straight line with a positive slope, as observed elsewhere [19,21,22,42].

As seen in Figs. 7–10, the strain-hardening rate always decreased rapidly with strain near the onset of necking. If the strain-hardening rate continues to decrease during necking at the same rate, it will become a small positive value or more likely a negative value at the fracture strain. However, the high positive HRN values displayed in Fig. 12 indicates that this prediction is invalid [19]. Since HRN turned out to be approximately the same as PIS, the downward curve for strain-hardening rate near the onset of necking, in Figs. 7–10, must change to a horizontal line during necking deformation. Two reasons for attaining and maintaining such high strain-hardening rates during plastic instability have been suggested by the present authors [19,21,22]:

First, a multi-axial stress state is developed in the necked region [19,42,45]. Since the true stress for a neck is calculated by dividing applied load by cross-sectional area, the stress was the axial component of a multi-axial stress field, i.e., the stress component in the loading direction. This axial stress component is dependent on the geometry of the neck, while the equivalent stress is a more genuine stress response of the material and is nearly independent of specimen geometry. Both the axial and equivalent stresses should be the same during uniform deformation cans where the transverse components are zero. In necking deformation, however, triaxial stress components are generated to accommodate the necked geometry. Since the constraint at the neck increases as necking proceeds, the axial stress component needed to deform the specimen can be higher than the equivalent stress at a given strain [19,23,28]. Therefore, the HRN, which is defined as the strain-derivative of the axial stress component, can also

Fig. 12. Variation of plastic instability stress (PIS) with test temperature and comparison with average strain-hardening rate during necking (HRN).

be higher than the strain-derivative of equivalent stress. (Note that the true strain in the loading direction is identical with the equivalent strain in the axi-symmetrical condition.)

Secondly, the complexities of geometry and stress state in the necked region will activate additional dislocation slip systems or even different deformation mechanisms in the material. This can also help to sustain a high strain-hardening rate in the loading direction, which usually falls during uniform deformation. If the strain-hardening rate is calculated for the equivalent stress, it would continue to decrease after the onset of necking although the PIS values are similar to the HRN values. Thus the apparently constant HRN is believed to result from a delicate balance between two effects: (a) the decreasing load carrying capability due to area contraction and reduction in hardening rate in the equivalent stress term and (b) the increasing constraint effect from increasing stress triaxiality.

3.5. A common criterion for plastic instability after pre-strain and irradiation

Recent analyses of the plastic instability behavior of numerous irradiated polycrystalline metals [21,22] showed that necking at yield occurred when the YS was above the PIS of the unirradiated material. This invariance of PIS was also confirmed by the observation that the true stress–true strain curves for irradiated materials could be superimposed on the curves for unirradiated materials by shifting along the strain axis until coincidence of stress was reached [21,22,42–44]. These results led to the conclusion that the two different microstructures resulting from radiation-induced defects and deformation-produced dislocations, produced similar net effects on strain-hardening behavior. It was also suggested that thins insensitivity of strain-hardening behavior and PIS to the original microstructures was a general phenomena for many metallic materials hardened by any defect structures, provided the matrix strength was not significantly modified during generation of those defects [21]. In the present study, this concept is further validated for dislocation-hardened or pre-strained materials. In Fig. 13, the PIS of annealed 316LN steel is compared with the YS of 20% cold-worked 316LN steel, where dislocations have been introduced by cold rolling at room temperature. The PIS values for annealed 316LN material are 810, 690, and 610 MPa at 100, 200, and 400 °C, respectively. The later two PIS values are nearly the same as the YS values for the 20% cold-worked 316 steel at corresponding temperatures. At or below 100 °C the YS of 20% cold-worked 316LN steel was always lower than the PIS and, as predicted, necking at yield did not occur (see Fig. 4). Meanwhile, above 100 °C, when the YS of the 20% cold-worked steel became equal to the PIS values of the an-
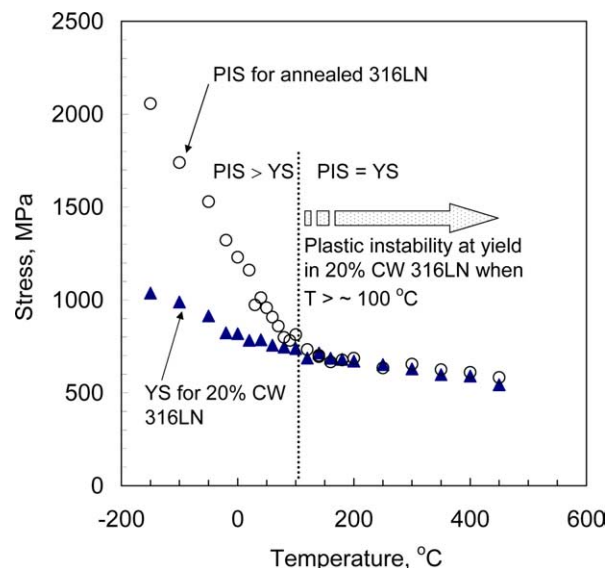

Fig. 13. Comparison of yield stress (YS) and plastic instability stress (PIS) in 20% cold-worked and annealed 316LN stainless steels.

nealed steel, the 20% cold-worked specimens always showed prompt necking at yield.

It is also worth mentioning that the YS after 20% cold work dose not exceed the PIS of annealed material, as seen in Fig. 13. This means that the maximum YS after pre-strain is bounded by the PIS of the annealed material. In contrast to this pre-strained material case, the YS values of irradiated metals continued to increase with irradiation dose and exceeded the PIS values after critical doses [21,22]. This behavior may originate from differences in the characteristics and effects of the two defect types, strain-induced tangled dislocations and radiation-induced defect clusters. The radiation-induced defects apparently act as obstacles for extending the elastic limit above the PIS by increasing the critical stress for yielding; thereafter, highly localized strain in the form of dislocation channeling renders the obstacles transparent to the passage of glide dislocations. Preexisting dislocations act as obstacles to additional dislocation glides and they, or their segment, can continue to glide under elevated stresses even if the test temperature differs from the cold-working temperature. Since the deformation at elevated temperature is a continuation of that at lower temperature, it will be subjected to the plastic instability criterion once the YS of the cold-worked steel reaches the PIS of the annealed material. This results in the fact that the YS of the cold-worked steel cannot exceed the PIS of the annealed material [21].

4. Conclusions

Strain-hardening and plastic-instability behavior was investigated for annealed and cold-worked austenitic

stainless steels in the temperature range −150 to 450 °C. The following conclusions are drawn from this work:

1. In both annealed and cold-worked conditions the strength of stainless steels decreased with increasing temperature, while ductility peaked at room temperature or below.

2. Above room temperature the true strain-hardening rate decreased monotonically with strain in the uniform deformation region. At room temperature or below, however, the strain-hardening rate showed two-stage hardening behavior; it decreased with strain below 3–20% and then it experienced an additional increase-decrease cycle before plastic instability. This characteristic two-stage hardening was explained by the stress-induced transformation of austenite to martensite.

3. The plastic instability stress (PIS) was independent of cold work before testing, and the cold-worked specimens failed by prompt necking at yield when the yield stress reached the PIS of annealed material. This plastic instability behavior after pre-strain resembled that of irradiated polycrystalline metals.

4. The average strain-hardening rate during necking (HRN) was almost the same as the PIS, which was much higher than the predicted (or extrapolated) value based on the strain-hardening rate curve before plastic instability. The reason for retaining high, constant HRN value is proposed to be determined by a balance between two effects: (a) the decreasing load carrying capability due to cross-section area contraction and reduction in hardening rate in the equivalent stress–strain response and (b) the increasing constraint effect from increasing stress triaxiality in the neck.

5. The strain-hardening behavior during necking was nearly independent of the microstructure of the material, but it was strongly dependent on temperature. Although both pre-straining (cold work) and irradiation strengthen the material, they do not change the mechanical behavior at or after the onset of necking.

Acknowledgements

References

[1] Source book on stainless steels. Am Soc Met; 1976.
[2] Lula RA. Stainless steel. Am Soc Met 1966;15.
[3] Roberts JTA. Structural materials in nuclear power system. Plenum Pub Co; 1981.
[4] Ma BM. Nuclear reactor materials and applications. Van Nostrand Reinhold Co; 1983.
[5] Sencer BH, Was GS, Sagisaka M, Isobe Y, Bond GM, Garner FA. J Nucl Mater 2003;323:18.
[6] Garner FA, Toloczko MB. J Nucl Mater 1997;251:252.
[7] Pawel JE, Rowcliffe AF, Lucas GE, Zinkle SJ. J Nucl Mater 1996;239:261.
[8] Pawel JE, Rowcliffe AF, Alexander DJ, Grossbeck ML, Shiba K. J Nucl Mater 1996;233–237:202.
[9] Rowcliffe AF, Zinkle SJ, Stubbins JF, Edwards DJ, Alexander DJ. J Nucl Mater 1998;258–263:183.
[10] Lucas GE, Billone M, Powel JE, Hamilton ML. J Nucl Mater 1996;233–237:207.
[11] Beryakov VA, Fabristsiev SA, Mazul IV, Rowcliffe AF. J Nucl Mater 2000;283:962.
[12] Hashimoto N, Zinkle SJ, Rowcliffe AF, Robertson JP, Jitsukawa S. J Nucl Mater 2000;283:528.
[13] Farrell K, Byun TS. Spallation neutron source project report: SNS/TSR-193, Oak Ridge National Lab; 2000.
[14] Mansur LK. J Nucl Mater 2003;318:14.
[15] Farrell K, Byun TS. J Nucl Mater 2001;296:129.
[16] Maloy SA, James MR, Willcutt G, Sommer WF, Sokolov M, Snead LL, Hamilton ML, Garner FA. J Nucl Mater 2001;296:119.
[17] Maloy SA, James MR, Johnson WR, Byun TS, Farrell K, Toloczko MB. J Nucl Mater 2003;318:283.
[18] Byun TS, Farrell K, Lee EH, Hunn JD, Mansur LK. J Nucl Mater 2001;298:269.
[19] Byun TS, Farrell K, Lee EH, Mansur LK, Maloy SA, James MR, Johnson WR. J Nucl Mater 2002;303:34.
[20] Farrell K, Mansur LK. Materials selection considerations for the Oak Ridge Spallation Neutron Source (ORSNS). In: Mansur LK, Ullmaier H, editors. Proceedings of the International Workshop on Spallation Materials Technology, Oak Ridge, TN, USA; 1996.
[21] Byun TS, Farrell K. Acta Mater 2004;52:1597.
[22] Byun TS, Farrell F, Hashimoto N. Plastic instability behavior of bcc and hcp metals after low temperature neutron irradiation. J Nucl Mater [in press].
[23] Dieter GE. Mechanical metallurgy. third ed. McGraw-Hill Book Co; 1986.
[24] Meyers MA, Chawla KK. Mechanical behavior of materials. Prentice-Hall Inc; 1998.
[25] Hertzberg RW. Deformation and fracture mechanics of engineering materials. John Wiley & Sons, Inc; 1989.
[26] Hirth JP, Lothe J. Theory of dislocations. McGraw-Hill Book Co; 1968.
[27] Honeycombe RWK, Steels, microstructures and properties, ASM Metallurgy and Materials Science Series, Edward Arnold Ltd; 1982.
[28] Brooks JW, Loretto MH, Smallman RE. Acta Metall 1979;27:1829.
[29] Brooks JW, Loretto MH, Smallman RE. Acta Metall 1979;27:1839.
[30] Cottrell AH. An introduction to metallurgy. Edward Arnold Ltd; 1975.
[31] Goodchild D, Roberts WD, Wilson DV. Acta Metall 1970;18:1137.
[32] Kelly A, Groves GW. Crystallography and crystal defects. J.D. Arrowsmith Ltd; 1970.
[33] Murr LE. Interfacial phenomena in metals and alloys. Reading, MA: Addision-Wesley Co; 1975.
[34] Byun TS, Lee EH, Hunn JH. J Nucl Mater 2003;321:29.
[35] Byun TS. Acta Mater 2003;51:3063.
[36] Copley SM, Kear BH. Acta Metall 1968;16:227.
[37] Kestenbach HJ. Philos Mag 1977;36:1509.

[38] Odette GR, He MY, Donahue EG, Spätig P, Tamamoto T. J Nucl Mater 2002;307–311:171.

[39] Grössel O, Frommeyer G. Mater Sci Technol 1998;14: 1213.

[40] Grössel O, Kruger L, Frommeyer G, Meyer LW. Int J Plasticity 2000;16:10.

[41] Brux U, Frommeyer G, Grössel O, Meyer LW, Weise A. Steel Res 2002;73:294.

[42] van Osch EV, DeVries MI. J Nucl Mater 1999;271 & 272:162.

[43] Ohr SM. Scr Metall 1968;2:213.

[44] Mogfold IL, Hull D. J Iron Steel Inst 1963;201:55.

[45] Aronofsky J. J Appl Mech 1951;18:75.